ARTICLES
https://doi.org/10.1038/s41565-018-0284-y
nature nanotechnology

# In situ quantification of interphasial chemistry in Li-ion battery

Tongchao Liu[1,2,5], Lingpiao Lin[1,5], Xuanxuan Bi[2], Leilei Tian[1], Kai Yang[1], Jiajie Liu[1], Maofan Li[1], Zonghai Chen[2], Jun Lu[2*], Khalil Amine[2,4*], Kang Xu[3*] and Feng Pan[1*]

**The solid–electrolyte interphase (SEI) is probably the least understood component in Li-ion batteries. Considerable effort has been put into understanding its formation and electrochemistry under realistic battery conditions, but mechanistic insights have mostly been inferred indirectly. Here we show the formation of the SEI between a graphite anode and a carbonate electrolyte through combined atomic-scale microscopy and in situ and operando techniques. In particular, we weigh the graphitic anode during its initial lithiation process with an electrochemical quartz crystal microbalance, which unequivocally identifies lithium fluoride and lithium alkylcarbonates as the main chemical components at different potentials. In situ gas analysis confirms the preferential reduction of cyclic over acyclic carbonate molecules, making its reduction product the major component in the SEI. We find that SEI formation starts at graphite edge sites with dimerization of solvated $Li^+$ intercalation between graphite layers. We also show that this lithium salt, at least in its nascent form, can be re-oxidized, despite the general belief that an SEI is electrochemically inert and its formation irreversible.**

Although Li-ion batteries (LIBs) are ubiquitous[1,2], much of the electrochemical processes governing their chemistry remains unclear. In particular, the solid–electrolyte interphase (SEI) is probably the most elusive component[3,4]. To maximize energy densities, the electrodes in LIBs are designed to operate at extreme potentials[5,6], so electrolytes need to work under electrochemical strains far beyond their thermodynamic stability limits at both the anode and cathode surfaces. In such hostile environments, the kinetic stability of electrolytes is often achieved through a passivation process, where trace amounts of electrolyte components decompose and form a dense and protective layer on the electrode surfaces[6,7]. This passivation layer must protect the electrode from electron tunnelling but remain conductive to $Li^+$ ions[8]. It is this SEI that ensures the reversibility and rate-capability of LIB chemistries[9,10].

Given its importance, the SEI has been extensively studied with a number of analytical tools, both ex situ and in situ[3,9,11]. The former, represented by X-ray photoelectron spectroscopy (XPS)[12,13], scanning and transmission electron microscopy (SEM and TEM)[14,15] or secondary ion mass spectroscopy (SIMS)[16], provide critical chemical and morphological information, but artefacts might inadvertently be present due to the high-energy photon or electron beams used. Moreover, sample preparation might alter or contaminate the interphase. The latter, for example, atomic force microscopy (AFM)[17–19] and electrochemical impedance spectroscopy (EIS)[20], although non-destructive to surfaces, are often phenomenological tools that cannot provide quantitative insights into the underlying chemistry. Quantitative detection of the SEI components has therefore been challenging. Recent efforts[21,22] in developing in situ and operando techniques based on TEM or XPS have enabled the direct visualization of battery components during their electrochemical operation, but either the temporal or spatial resolution is insufficient to characterize the interphase. In most cases, non-standard electrolyte systems (such as ionic liquids) have had to be adopted, because vacuum conditions are required for sample visualization. Finally, the non-crystalline and composite nature of the SEI further complicates interpretation of the interphasial chemistries.

In this work, we describe a concerted approach to quantitatively monitor the interphasial components as they evolve on the electrode surface at various potentials. Integrating the quantitative and in situ and operando natures of the electrochemical quartz crystal microbalance (EQCM) and the atomistic precision of AFM (Supplementary Figs. 1–4), we study a graphitic electrode while cathodically polarized in a typical electrolyte composition (1.0 M $LiPF_6$ dissolved in an equimolar mixture of ethylene carbonate (EC) and dimethyl carbonate (DMC)). As a highly sensitive mass monitoring technique[23–25], EQCM allows us to precisely weigh what species are accumulated on or lost from the graphite electrode as a function of the applied potential, while AFM images reveal how the highly oriented pyrolytic graphite (HOPG) interacts with the solvated $Li^+$ during the initial lithiation and delithiation processes. These quantitative observations enable us to establish an atomistic picture for the formation mechanism of the SEI that has been hitherto unavailable.

## Weighing the SEI

When a graphite anode is gradually polarized towards the potential of Li metal, a series of reactions occur before $Li^+$ intercalation, including the initial formation of the SEI. Based on the mass change recorded by EQCM during this process, we can divide the cathodic polarization of graphite into four regions (Fig. 1a). Region I lies between the open-circuit voltage (OCV, see Methods) and 2.4 V, where both current and mass change remain essentially in the background. Region II, between 2.4 and 1.1 V, where the current starts to depart from the baseline and reaches a local maximum at 1.6 V, indicates the onset of certain reactions accompanied by a mass

[1]School of Advanced Materials, Peking University, Shenzhen Graduate School, Shenzhen, China. [2]Chemical Sciences and Engineering Division, Argonne National Laboratory, Argonne, IL, USA. [3]Electrochemistry Branch, Sensor and Electron Devices Directorate, Power and Energy Division, US Army Research Laboratory, Adelphi, MD, USA. [4]Material Science and Engineering, Stanford University, Stanford, CA, USA. [5]These authors contributed equally: Tongchao Liu and Lingpiao Lin. *e-mail: junlu@anl.gov; amine@anl.gov; conrad.k.xu.civ@mail.mil; panfeng@pkusz.edu.cn

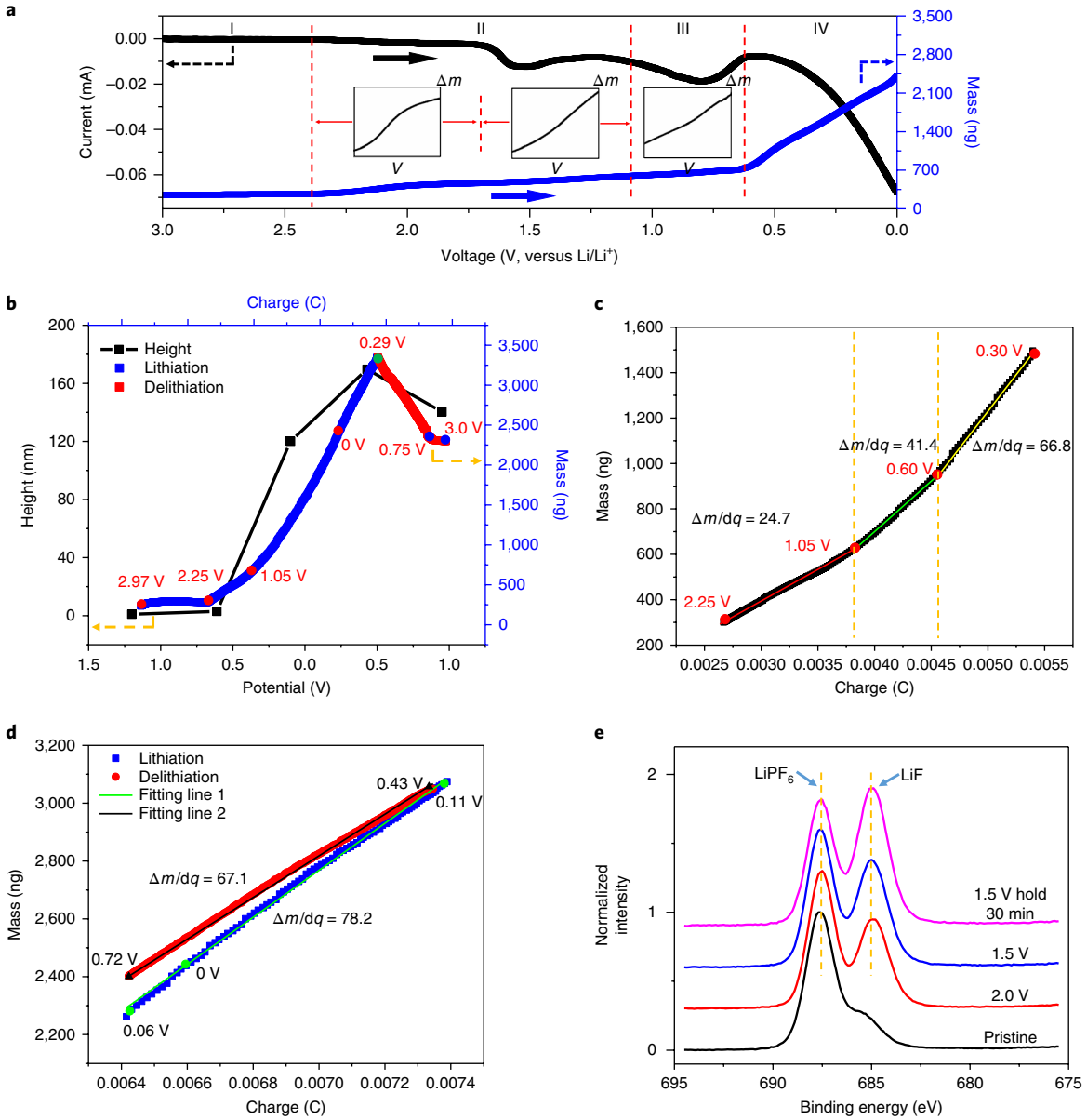


**Fig. 1 | In situ, operando and quantitative characterization of live formation and chemistry of the SEI on graphite. a**, Cyclic voltammetry cathodic scan (black) of the fresh graphite electrode in 1 mol $l^{-1}$ $LiPF_6$ EC/DMC at 1 mV $s^{-1}$ from OCV (3.0 V) to 0.0 V, and the simultaneous responses of the deposition on the graphite electrode (blue) as recorded by EQCM. Solid black and blue arrows represent scan directions for cyclic voltammetry and EQCM, respectively. **b**, Matched mass and height change during the cathodic scan and anodic scan process. **c**, Mass versus charge curve in the voltage range 2.25–0.30 V, and slopes ($\Delta m/dq$) converted into g $mol^{-1}$ $e^-$ for convenience of understanding. **d**, Mass versus charge curve for SEI formation (blue line) and SEI re-oxidation (red line) in the first cycle. **e**, Chemical analysis of the interphase via F 1s XPS spectra, where black, red, blue and purple curves correspond to the pristine electrode, electrode discharged at 2.0 V, electrode discharged at 1.5 V and electrode discharged at 1.5 V and held for 30 min, respectively.

change. In region III, between 1.1 and 0.74 V, there is a broad current response corresponding to the initial reduction of electrolyte components. Region IV, between 0.74 and 0.0 V, where major electrochemical reduction of the intercalated species occurs, marks the exclusive decomposition of the liquid electrolyte (alkylcarbonate esters) to form the eventual SEI.

During this main formation process of the interphase, EQCM registers the mass change ($\Delta m$) versus charge change ($dq$) in the graphite electrode attached to the quartz surface, with a relative accuracy of ±1.34 ng. Such a change should follow the Sauerbrey equation[26] (Supplementary Section 2). The curve of mass versus charge can be divided into three parts (Fig. 1b,c). From 2.25 to 1.05 V, the mass change per electron $\Delta m/dq = 24.7$ g $mol^{-1}$ of $e^-$, which is rather close to the formula mass of LiF (25.9 g $mol^{-1}$), indicating that this inorganic species is dominating the surface reaction in this range. LiF formation is believed to be directly associated with $PF_6^-$ hydrolysis in the presence of trace water via the reaction in equation (1)[11]. Note that this is a chemical rather than an electrochemical reaction. As we detect its formation by EQCM, LiF should, at least partially, be generated via an alternative electrochemical pathway. Combined with the differential electrochemical mass spectrum (DEMS) (Fig. 2a), which detects $H_2$ production, we posit that equation (2) is responsible for the electrochemical formation of LiF. This hypothesis is also supported by XPS measurements

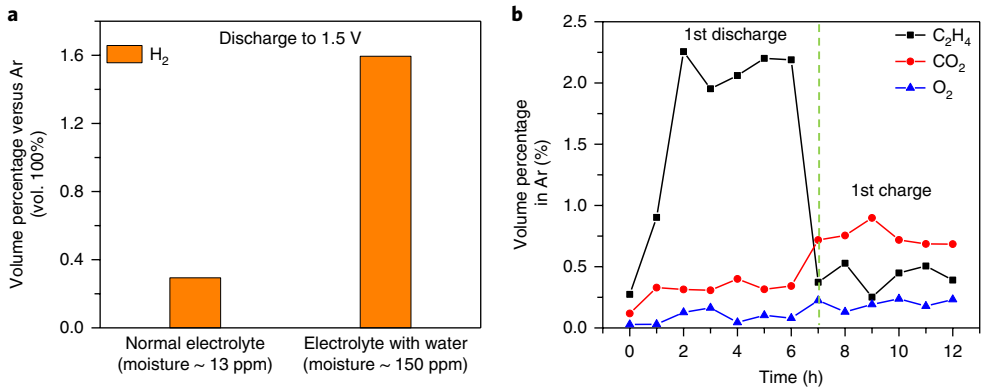


**Fig. 2 | In situ differential electrochemical mass spectroscopy measurements performed on the graphite electrode during SEI formation. a**, Gas generated from a normal electrolyte (moisture of 13 ppm, see 'Materials' in Supplementary Section 1) and a moist electrolyte (water level of 150 ppm) during discharge from OCV (~3.0 V) to 1.5 V. **b**, Accumulated gas generation during the first lithiation and delithiation of a graphite/$LiFePO_4$ full cell at C/5 (the C-rate is a measure of the rate at which a battery is charged/discharged relative to its maximum capacity; at C/5 rate, the charge/discharge current will charge/discharge the entire battery in 5 hours). Green dashed line separates the first discharge from first charge.

(Fig. 1e), in which the LiF signal increases with the voltage held at 1.5 V for ~30 min. Trace water in the electrolyte serves as a catalyst for LiF formation, through either equation (1) or equation (2) (note that HF is generated from equation (1)).

$$LiPF_6 + H_2O \longrightarrow 2HF + POF_3 + LiF \quad (1)$$

$$HF + Li^+ \xrightarrow{e^-} 0.5H_2 + LiF \quad (2)$$

To confirm the above hypothesis, we prepared a control electrolyte with 400 ppm water. The current and mass rapidly increase in the EQCM curve (Supplementary Fig. 5), and this is accompanied by simultaneous LiF signal increase in XPS (Supplementary Fig. 6). Moreover, we detected $H_2$ generation by DEMS when holding the graphite at 1.5 V in the control electrolyte (Fig. 2a). Interestingly, $H_2$ generation increased by a factor of approximately four after the deliberate addition of 150 ppm water, a proof that $H_2$ generation directly relies on the hydrolysis of $PF_6^-$. The absence of ethylene ($C_2H_4$) at 1.5 V indicates that the typical electrochemical reduction of these carbonate molecules has not yet occurred.

Between 1.05 and 0.60 V (Fig. 1c), $\Delta m/dq$ increases to 41.4, and eventually stabilizes at 66.8 between 0.60 and 0.3 V. This growth suggests that the SEI ingredients start to shift from neat inorganic LiF ($\Delta m/dq = 25.9$) to a more diversified and organic interphasial composition. Finally, when the potential drops under 0.1 V, $\Delta m/dq$ reaches 78.2 (Fig. 1d), a value close to the mass/charge ratio ($m/e$) of lithium alkylcarbonates, which are the single-electron reduction products from both carbonate solvent molecules:

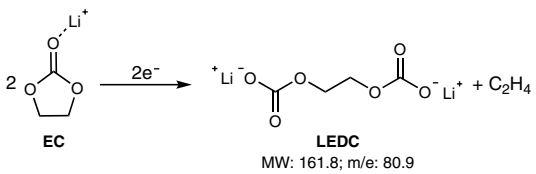


(3)

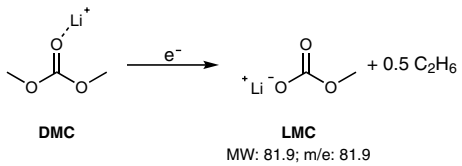


(4)

Considering that we used an electrolyte based on an EC/DMC mixture, the reduction of both EC and DMC can occur simultaneously[27,28], although it has been reported that EC reduction should be preferred[29,30]. Because $\Delta m/dq$ for lithium ethylene dicarbonate (LEDC, $C_4H_4O_6Li_2$ from EC reduction; $m/e = 80.9$, equation (3)) and lithium methylcarbonate (LMC, $C_2H_3O_3Li$ from DMC reduction; $m/e = 81.9$, equation (4)) differs by only 1 atomic unit, EQCM alone cannot differentiate which alkylcarbonate is predominately formed, or whether a preference exists at all. It should be further cautioned that, given the accuracy limit of EQCM, other organic species with similar molecular weights are also possible. Precisely identifying these species needs other complementary characterization means.

## Differentiating interphasial reactions

According to equations (3) and (4), what can reliably distinguish the single-electron reductions of EC and DMC lies in their respective gaseous products. Although the molecular weights of ethylene ($C_2H_4$, $M_w$ of 28) and ethane ($C_2H_6$, $M_w$ of 30) are still rather close, the precision of mass spectrometry should be able to highlight the difference. Thus, we used in situ DEMS (Supplementary Fig. 7) for a graphite electrode cathodically polarized in the same electrolyte during its initial lithiation/delithiation. The gaseous products from the cell were pumped into a mass spectrometer, where they were bombarded, and the resulting fragments were analysed for structural identification. A cluster of peaks were generated centering on an $m/e$ of ~25–30 (Supplementary Figs. 8 and 9), representing the complicated breakdown of the gaseous products under bombardment. By comparing the fragmentation patterns with the standard mass spectra from the National Institute of Standards and Technology (NIST)[31], which provides a fingerprint database for the identification of chemical compounds fragmented under a mass spectrometry environment, we attributed the species at $m/e$ 29 and 30 to DMC (Supplementary Figs. 10 and 11), which can escape from the electrochemical chamber into the DEMS line due to its volatility (b.p. 91 °C). The twin peaks at $m/e$ 29 and 30 thus should not be attributed to the ethane that is produced electrochemically by DMC reduction (Supplementary Fig. 8). The peak at $m/e$ 28 can be due to either ethylene ($C_2H_4$) produced by EC reduction or the dehydrogenated product of ethane ($C_2H_6$) produced by DMC reduction. However, a comparison of the relative ratios of the peaks at $m/e$ 26, 27 and 28 (Supplementary Fig. 8) against NIST standards (Supplementary Figs. 10, 12 and 13) conclusively points to the sole origin being EC reduction.

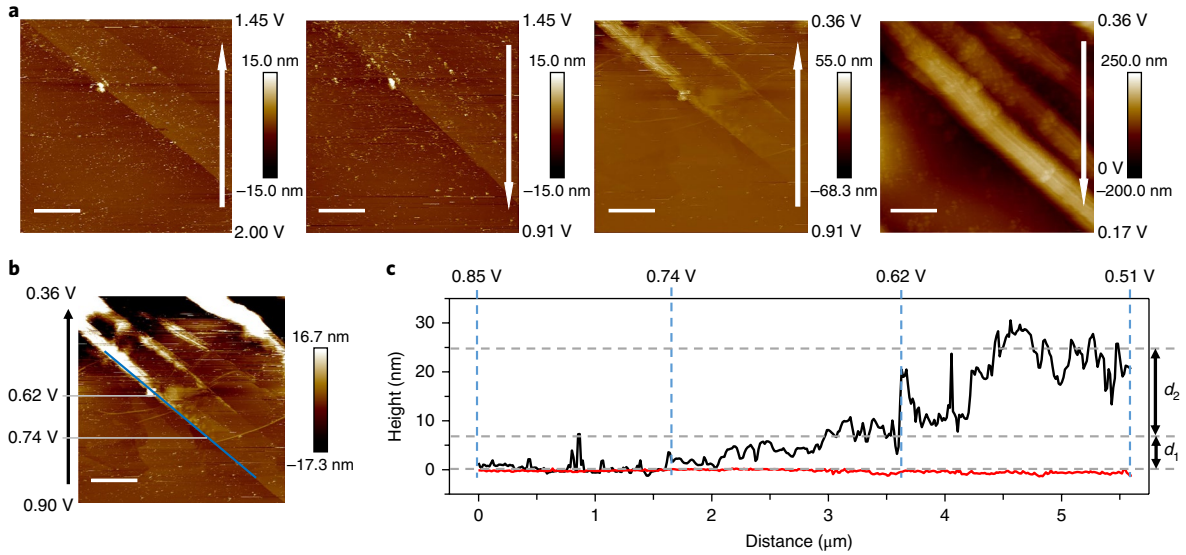


**Fig. 3 | Morphological observation of the SEI via in situ and operando AFM measurements during the first lithiation of HOPG. a**, Topological imaging of HOPG during the cyclic voltammetry cathodic scan from 2.0 V to 0, and then the anodic scan from 0 to 0.17 V, where the long white arrows indicate scan directions. Scale bars, 1.0 μm. **b**, Correlation of morphology and potential during the initial cathodic scan from 0.90 V to 0.36 V. Scale bar, 1.0 μm. The blue line is along the direction of the edge site. **c**, Height distribution (black curve) of the SEI on the stage labelled by the blue line in **b**, and the datum height line (red curve), extracted from the first image in **a**.

Based on both EQCM and DEMS, the alkylcarbonate produced at a potential below 0.3 V, as represented by the $\Delta m/\mathrm{d}q$ of 78.2 in EQCM, should be primarily generated from EC reduction (equation (3)). In addition, the increasing intensities of ethylene signature peaks (Supplementary Figs. 8 and 9) starting from 2 h (~0.67 V) also indicate that this process between 1.05 and 0.60 V should be attributed to solvent reduction.

## Dynamic formation of the interphase at the nanoscale

At the low potential of the initial lithiation near 0.10 V (Fig. 1d), the mass change nearly corresponds to neat LEDC deposition, suggesting that solvent reduction dominates the SEI formation process, with negligible $Li^+$ intercalation. The intercalation of neat $Li^+$ without solvent molecules can only occur in the presence of a fully formed interphase that seals off the edge sites of graphitic anodes. As expected, in the cycles following the initial lithiation, the mass change gradually approaches a constant value of 7.9 (Supplementary Fig. 14), which, within experimental error, matches the naked $Li^+$ value ($\Delta m/\mathrm{d}q$ 6.9).

We used different scan rates (0.1 and 1.0 mV $s^{-1}$) in the EQCM experiments to study how the densification of the SEI evolves with kinetics (Supplementary Fig. 15). At a slower rate, lower $\Delta m/\mathrm{d}q$ values are achieved at the same potential points. Considering that a perfect SEI should only allow naked $Li^+$ to intercalate ($\Delta m/\mathrm{d}q = 6.9$), these lower values quantify how effectively the solvent reduction reaction is blocked, or in other words how effective the protection function of the newly formed SEI is. A slow rate gives more time for solvent molecules to be reduced and assembled into a more densified interphase.

Morphological observation on the HOPG surface via AFM (Fig. 3 and Supplementary Fig. 16) reveals that tiny island-like features with irregular distributions start appearing below 2.0 V and continue to grow down to 0.91 V (Fig. 3a), corresponding to LiF generation as identified by EQCM (Fig. 1c) and XPS (Fig. 1e) in region II. Initial SEI formation occurs between 0.91 and 0.36 V (Fig. 3a). These main interphase components grow along the edge sites rather than on the basal planes of HOPG, consistent with the established belief that SEI formation is preceded, or even guided, by the co-intercalation of solvated $Li^+$, which can only occur at the edge sites[29,32]. These edge-site depositions continue to grow in thickness accompanied by an increase in step heights as the potential decreases towards 0.0 V. This growth is induced by further SEI generation from the reduction of those solvent molecules in the primary solvation sheath of $Li^+$ that co-intercalate into the graphitic structure in this potential region (Fig. 3a). At 0.74 V, numerous particles appear (Fig. 3b,c), which gradually develop into broader and higher blisters near the edges at 0.62 V. During this process the height increases by 8.8 nm ($d_1$). With the potential of HOPG dropping below 0.62 V, the step height increases by an additional ~20 nm ($d_2$). The first height increase corresponds to the reduction peak observed in region III (Fig. 1a), and should be attributed to the onset reduction of the already co-intercalated species (solvated $Li^+$) between the graphene layers. In other words, it is between 0.74 and 0.62 V that the SEI experiences its onset formation. The increased height below 0.62 V is caused by the simultaneous co-intercalation of more solvated $Li^+$ into graphene layers along with their reduction, as the nascent SEI is still permeable at this stage.

It is widely accepted that the lithiation of graphite occurs in stages[33], with stage 1 being the formation of the fully lithiated state of graphite ($LiC_6$). To investigate whether this stepwise mechanism also occurs during SEI formation, we selected a few spots on HOPG with a known number of stacked graphene layers (Supplementary Fig. 17 and Supplementary Table 1). We then monitored how these monolayer, bilayer and quadruple-layer steps respond to the potential during the initial formation of the SEI (from 1.13 V to 0.51 V). We observe that around 0.88 V, where the solvated $Li^+$ starts to co-intercalate but it is not yet subject to major reductive decomposition, the step height increases by ~1.3 nm for a monolayer step, ~6.1 nm for a bilayer step and ~20.0 nm for a quadruple-layer step. Of particular interest is the height increase of 1.3 nm for the monolayer step, which is close to what would be expected for the expanded interlayer distance of a single-layer graphene structure caused by a $Li^+$ solvated by four solvent molecules (1.56 nm)[34]. On average, the step height change in the bilayer step is three to four times more than that of the monolayer, while that in the quadruple-layer step is ~1.5–3 times more than that of the bilayer step. These ratios are not

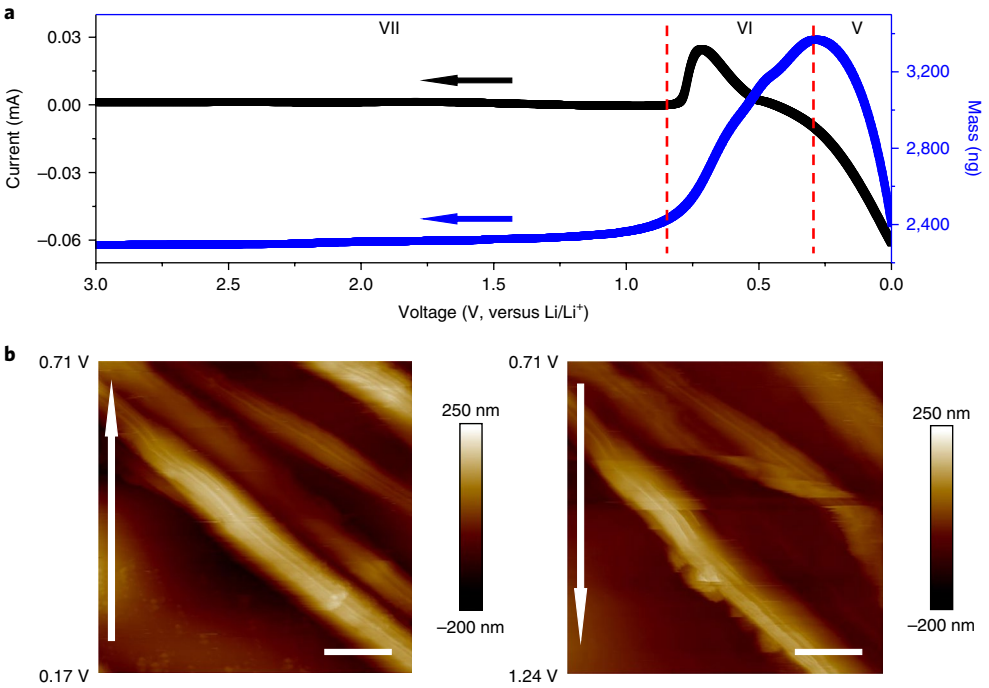


**Fig. 4 | Re-oxidation of the nascent interphase observed by EQCM and AFM. a**, Anodic scan of both cyclic voltammetry and EQCM curves of a graphite electrode in 1 M $LiPF_6$ EC/DMC at a scan rate of 1 mV $s^{-1}$. Solid black and blue arrows, respectively, represent the cyclic voltammetry and EQCM scan directions. **b**, AFM images of the SEI re-oxidation on HOPG with a cyclic voltammetry anodic scan from 0.17 to 1.24 V. Long white arrows indicate scan directions. Scale bars, 1.0 μm.

proportional to the number of steps, and suggest that the expansion of the graphene interlayer distance happens at the edge sites of every graphene layer without obvious sign of staging. When the electrode potential drops below 0.79 V, further height increases are induced due to the initial reduction and decomposition of co-intercalated solvated $Li^+$ (Supplementary Table 1). In the range of ~0.79–0.67 V, the step heights become constant and independent from the number of layers involved (Supplementary Table 1). This is because the decomposed solvent molecules arising from the already co-intercalated species (solvated $Li^+$) start to serve as nascent interphases at the edge sites of graphite, so additional solvated $Li^+$ can no longer be intercalated at this potential range, which is also consistent with the reduced reduction current we record around 0.6 V.

## Re-oxidation of the nascent interphase

Figure 4 summarizes the cyclic voltammetry, the mass change in EQCM (Fig. 4a) and surface morphology evolution on a HOPG electrode (Fig. 4b) during the anodic scan after the first lithiation process. The current remains cathodic between ~0 and 0.30 V (region V in Fig. 4a), indicating that SEI formation continues while the step height keeps increasing (Figs. 1b and 4b). In this region, the interphase continues to form through EC reduction (mass accumulation $\Delta m/\mathrm{d}q = 78.2$). Although this may appear to be counterintuitive, we must recall that what determines the nature of the reaction (reduction or oxidation) is the direction of the current flow, not the scan direction.

At ~0.30 V the current changes from cathodic to anodic (region VI in Fig. 4a), the step height of HOPG starts to decrease, and the formed interphase disappears (Fig. 4b). It has been reported that part of the surface deposits observed under AFM would completely disappear before a certain threshold value when the electrode potential is reversed; our observations confirm this interphasial re-oxidation mechanism[35]. To further study this peculiar process, we selected three spots on HOPG (Supplementary Fig. 18 and Supplementary Table 2): one with mostly the basal surface of HOPG and two with edge sites of four and two steps. The heights at these three spots were monitored during both lithiation (cathodic scan) and delithiation (anodic scan) processes (Supplementary Fig. 19 and Supplementary Table 3). While the step heights at both edge sites experience dramatic changes during the scan, the step height of the basal surface remains almost constant, because of its remote location from the intercalation reactions (the edge sites). Although all the heights never revert back to their pristine state, they clearly decrease in this voltage range. As a confirmation, the mass (Fig. 4a) also decreases in this range ($\Delta m/\mathrm{d}q = -67.1$; Fig. 1d), revealing loss of materials from the graphite surface. Such a mass loss is much larger than that of naked $Li^+$ ($\Delta m/\mathrm{d}q = 6.9$), indicating that at least part of the interphasial components are also lost. We posit that it is semi-carbonate resulting from EC reduction that generates this mass loss. A two-electron oxidation process is proposed below as a possible reaction pathway (equation (5)), which produces two molecules of $CO_2$ ($M_w$ of 44 g $mol^{-1}$), one molecule of ethylene ($C_2H_4$, $M_w$ of 28 g $mol^{-1}$) and half a molecule of oxygen ($O_2$, $M_w$ of 32 g $mol^{-1}$), the sum of which correspond to a total mass loss per electron of 66:

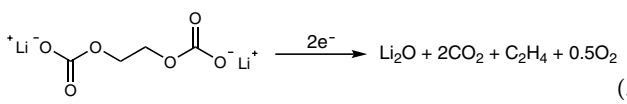


(5)

Therefore, in the very first delithiation cycle, the nascent interphase appeared to be partially re-oxidizable, leading to both gaseous and solid products. These observations could explain the reported meta-stability of the SEI ingredients in their nascent form.

We further scrutinized the above proposed mechanism with DEMS. As already shown in Fig. 2b, $C_2H_4$ is detected as the main gas generated in the first lithiation process of graphite, as expected from equation (3), with $CO_2$ and $O_2$ being around one-eighth of $C_2H_4$. During the charge (delithiation) process, however, the amount of $C_2H_4$ is significantly reduced, while $CO_2$ and $O_2$ slightly increase.

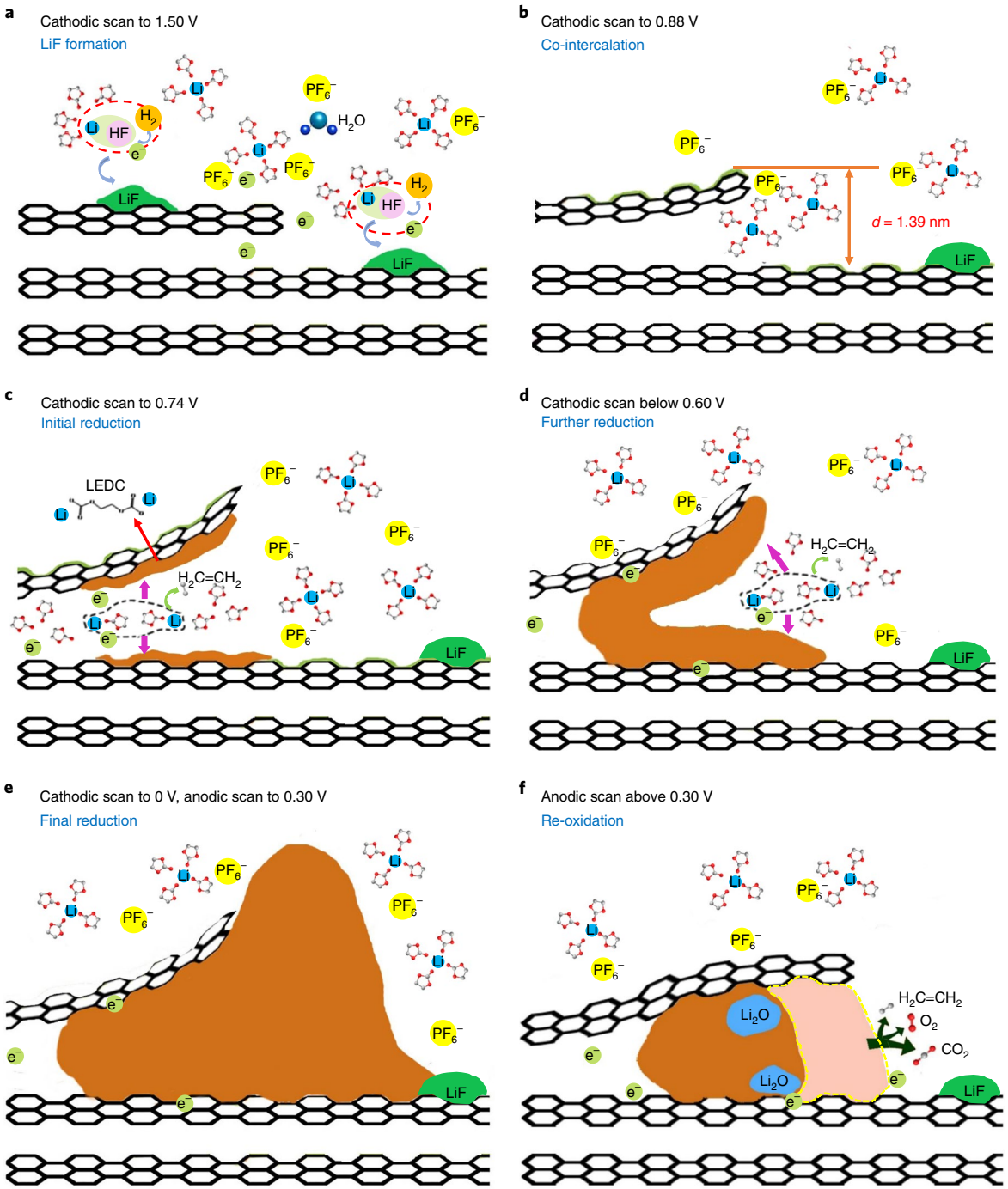


**Fig. 5 | Schematic illustration of the interphasial formation chemistry during the very first lithiation. a**, In the presence of trace $H_2O$ (which is always present in bulk electrolyte), HF (produced by $PF_6^-$ hydrolysis) starts to reductively decompose at ~1.5 V, resulting in an irregular deposition of LiF (equations (1) and (2)) on the graphite surface accompanied by $H_2$ generation. **b**, Solvated $Li^+$ with four EC molecules approaches the graphite edge site and starts to co-intercalate below 0.88 V, which forces the graphene interlayer distance to widen, leading to a transient rise in step height of >1.3 nm per graphene layer. **c**, Continuous populating of the graphene layers with solvated $Li^+$ further increases the height; however, a dramatic height increase occurs after 0.74 V, where EC reduction starts, generating both gaseous and organic lithium salt products such as LEDC. The former is responsible for the significantly swollen graphitic structure near edge sites, and the latter would remain on the graphite surface near edge sites as the main component of SEI, gradually blocking the entry of solvated $Li^+$. **d**,**e**, SEI formation continues when the cathodic scan drops below 0.6 V, with the SEI further densifying, until the current reverses direction with the anodic scan above 0.3 V. **f**, On reversal of the current to the anodic regime above 0.3 V, the lithium alkylcarbonates (LEDC) in nascent SEI start to be partially re-oxidized.

Moreover, the proportion of $CO_2$, $C_2H_4$ and $O_2$ is rather close to a 4:2:1 ratio, consistent with the mechanism proposed in equation (5). Further proofs (Supplementary Figs. 20–24) from TEM, chemical components analysis (Supplementary Fig. 25) from XPS, as well as a high-precision current measurement (Supplementary Fig. 26) all provide consistent support for the interphasial process as observed above.

## Conclusion

We have characterized the formation process of the solid–electrolyte interphase on graphitic electrode at the nanoscale. We hope that this level of detail can provide useful guidelines for designing and tailoring better interphases for new battery chemistries. We summarize the SEI formation in Fig. 5. There are five distinct chemical or electrochemical processes: (1) LiF formation at 1.5 V (Fig. 5a); (2) co-intercalation of $Li^+$ (solvent)$_x$ at 0.88 V (Fig. 5b); (3) initial EC reduction at 0.74 V (Fig. 5c); (4–5) major EC reduction at lower potentials (Fig. 5d,e); (6) lithium alkylcarbonates produced by EC reduction are partially re-oxidized during anodic scan above 0.3 V (Fig. 5f). The capability of the SEI to be re-oxidized seems to depend on its age: nascent SEI readily disappears on recharging, but it becomes more and more difficult to oxidize it on well-cycled electrodes. Further investigation is needed to explain the origin of this aging effect.

## Online content

Any methods, additional references, Nature Research reporting summaries, source data, statements of data availability, and associated accession codes are available at https://doi.org/10.1038/s41565-018-0284-y.

Received: 2 October 2017; Accepted: 20 September 2018;
Published online: 12 November 2018

## References

1. Chu, S., Cui, Y. & Liu, N. The path towards sustainable energy. *Nat. Mater.* **16**, 16–22 (2017).
2. Lu, J. et al. The role of nanotechnology in the development of battery materials for electric vehicles. *Nat. Nanotech.* **11**, 1031–1038 (2016).
3. Xu, K. Electrolytes and interphases in Li-ion batteries and beyond. *Chem. Rev.* **114**, 11503–11618 (2014).
4. Winter, M. The solid electrolyte interphase—the most important and the least understood solid electrolyte in rechargeable Li batteries. *Z. Phys. Chem.* **223**, 1395–1406 (2009).
5. Nitta, N., Wu, F., Lee, J. T. & Yushin, G. Li-ion battery materials: present and future. *Mater. Today* **18**, 252–264 (2015).
6. Goodenough, J. B. & Kim, Y. Challenges for rechargeable Li batteries. *Chem. Mater.* **22**, 587–603 (2009).
7. Hu, L. & Xu, K. Nonflammable electrolyte enhances battery safety. *Proc. Natl Acad. Sci. USA* **111**, 3205–3206 (2014).
8. Peled, E. The electrochemical behavior of alkali and alkaline earth metals in nonaqueous battery systems—the solid electrolyte interphase model. *J. Electrochem. Soc.* **126**, 2047–2051 (1979).
9. An, S. J. et al. The state of understanding of the lithium-ion-battery graphite solid electrolyte interphase (SEI) and its relationship to formation cycling. *Carbon* **105**, 52–76 (2016).
10. Peled, E. & Menkin, S. SEI: past, present and future. *J. Electrochem. Soc.* **164**, A1703–A1719 (2017).
11. Xu, K. Nonaqueous liquid electrolytes for lithium-based rechargeable batteries. *Chem. Rev.* **104**, 4303–4417 (2004).
12. Lindgren, F. et al. SEI formation and interfacial stability of a Si electrode in a LiTDI-salt based electrolyte with FEC and VC additives for Li-ion batteries. *ACS Appl. Mater. Interfaces* **8**, 15758–15766 (2016).
13. Andersson, A., Henningson, A., Siegbahn, H., Jansson, U. & Edström, K. Electrochemically lithiated graphite characterised by photoelectron spectroscopy. *J. Power Sources* **119**, 522–527 (2003).
14. Andersson, A. & Edström, K. Chemical composition and morphology of the elevated temperature SEI on graphite. *J. Electrochem. Soc.* **148**, A1100–A1109 (2001).
15. Nie, M. et al. Lithium ion battery graphite solid electrolyte interphase revealed by microscopy and spectroscopy. *J. Phys. Chem. C* **117**, 1257–1267 (2013).
16. Peled, E. et al. Composition, depth profiles and lateral distribution of materials in the SEI built on HOPG-TOF SIMS and XPS studies. *J. Power Sources* **97**, 52–57 (2001).
17. Domi, Y. et al. Irreversible morphological changes of a graphite negative-electrode at high potentials in LiPF6-based electrolyte solution. *Phys. Chem. Chem. Phys.* **18**, 22426–22433 (2016).
18. Wang, L., Deng, D., Lev, L. C. & Ng, S. In-situ investigation of solid–electrolyte interphase formation on the anode of Li-ion batteries with atomic force microscopy. *J. Power Sources* **265**, 140–148 (2014).
19. Zhang, J. et al. Direct observation of inhomogeneous solid electrolyte interphase on MnO anode with atomic force microscopy and spectroscopy. *Nano Lett.* **12**, 2153–2157 (2012).
20. Yang, T., Sang, L., Ding, F., Zhang, J. & Liu, X. Three- and four-electrode EIS analysis of water stable lithium electrode with solid electrolyte plate. *Electrochem. Acta* **81**, 179–185 (2012).
21. Huang, J. Y. et al. In situ observation of the electrochemical lithiation of a single $SnO_2$ nanowire electrode. *Science* **330**, 1515–1520 (2010).
22. Zhang, C. et al. Measuring fundamental properties in operating solid oxide electrochemical cells by using in situ X-ray photoelectron spectroscopy. *Nat. Mater.* **9**, 944–949 (2010).
23. Griffin, J. M. et al. In situ NMR and electrochemical quartz crystal microbalance techniques reveal the structure of the electrical double layer in supercapacitors. *Nat. Mater.* **14**, 812–819 (2015).
24. Shpigel, N. et al. In situ hydrodynamic spectroscopy for structure characterization of porous energy storage electrodes. *Nat. Mater.* **15**, 570–575 (2016).
25. Song, X. et al. In-situ mass-electrochemical study of surface redox potential and interfacial chemical reactions of Li (Na) $FePO_4$ nanocrystals for Li (Na)-ion batteries. *Nano Energy* **37**, 90–97 (2017).
26. Jensen, K., Kim, K. & Zettl, A. An atomic-resolution nanomechanical mass sensor. *Nat. Nanotech.* **3**, 533–537 (2008).
27. Single, F., Horstmann, B. & Latz, A. Revealing SEI morphology: in-depth analysis of a modeling approach. *J. Electrochem. Soc.* **164**, E3132–E3145 (2017).
28. Single, F., Horstmann, B. & Latz, A. Dynamics and morphology of solid electrolyte interphase (SEI). *Phys. Chem. Chem. Phys.* **18**, 17810–17814 (2016).
29. Xu, K., Lam, Y., Zhang, S. S., Jow, T. R. & Curtis, T. B. Solvation sheath of $Li^+$ in nonaqueous electrolytes and its implication of graphite/electrolyte interface chemistry. *J. Phys. Chem. C* **111**, 7411–7421 (2007).
30. Zhuang, G. V., Xu, K., Yang, H., Jow, T. R. & Ross, P. N. Lithium ethylene dicarbonate identified as the primary product of chemical and electrochemical reduction of EC in 1.2 M $LiPF_6$/EC:EMC electrolyte. *J. Phys. Chem. B* **109**, 17567–17573 (2005).
31. Linstrom, P. J. & Mallard, W. *NIST Chemistry Webbook, NIST Standard Reference Database No. 69* (NIST, 2001).
32. Xu, K. 'Charge-transfer' process at graphite/electrolyte interface and the solvation sheath structure of $Li^+$ in nonaqueous electrolytes. *J. Electrochem. Soc.* **154**, A162–A167 (2007).
33. Dahn, J. R. Phase diagram of $Li_xC_6$. *Phys. Rev. B* **44**, 9170–9177 (1991).
34. Wagner, M., Albering, J., Moeller, K.-C., Besenhard, J. & Winter, M. XRD evidence for the electrochemical formation of $Li_+(PC)_yC_{n-}$ in PC-based electrolytes. *Electrochem. Commun.* **7**, 947–952 (2005).
35. Cresce, Av, Russell, S. M., Baker, D. R., Gaskell, K. J. & Xu, K. In situ and quantitative characterization of solid electrolyte interphases. *Nano Lett.* **14**, 1405–1412 (2014).

## Acknowledgements

This research was supported financially by the National Materials Genome Project (2016YFB0700600), the Guangdong Innovation Team Project (no. 2013N080) and Shenzhen Science and Technology Research Grants (nos. JCYJ20151015162256516, JCYJ20150729111733470 and JCYJ20160226105838578). J.Lu and K.A. acknowledge support from the US Department of Energy under contract no. DE-AC0206CH11357 with the main support provided by the Vehicle Technologies Office, Department of Energy (DOE) Office of Energy Efficiency and Renewable Energy. Support provided by the China Scholarship Council (CSC) during a visit of T.L. to Argonne National Laboratory is acknowledged.

## Author contributions

F.P., K.X., K.A. and T.L. conceived the work and designed the experiments. L.L., L.T. and K.Y. carried out the in situ AFM results. T.L., X.B., Z.C. and J. Lu performed the electrochemical measurements. T.L., J. Liu and M.L. conducted the TEM measurements. K.A., J. Lu, F.P. and K.X. wrote the manuscript, and all authors edited the manuscript.

## Competing interests

The authors declare no competing interests.

## Additional information

**Supplementary information** is available for this paper at https://doi.org/10.1038/s41565-018-0284-y.

**Reprints and permissions information** is available at www.nature.com/reprints.

**Correspondence and requests for materials** should be addressed to J.L. or K.A. or K.X. or F.P.

**Publisher's note:** Springer Nature remains neutral with regard to jurisdictional claims in published maps and institutional affiliations.

## Methods

**AFM.** In situ and operando AFM measurements were performed using a Nanoscope V, MultiMode instrument (Bruker AXS) placed in a glovebox. The tapping mode was used to collect all images with a single ScanAsyst-Fluid silicon probe (force constant of 0.7 N $m^{-1}$, Bruker). The resonance frequency of this cantilever was ~150 kHz. The images were captured in the retrace direction at a scan rate of 0.5 Hz. The scan size was 2,000 × 2,000 nm with an aspect ratio of 1:1 and an image resolution of 512 samples per line. The liquid cell with electrochemistry set-up was designed by Bruker AXS (Supplementary Fig. 2). HOPG with an extremely smooth surface was used as the working electrode to probe the dynamic reactions and morphology changes, and Li metal was used as the reference electrode and counterelectrode. Simultaneous electrochemical tests were conducted using a CHI 660E instrument (Shanghai Chenhua) at a scan rate of 1 mV $s^{-1}$ in the voltage range 0–3.0 V (OCV is 2.55 V for HOPG in the electrochemistry set-up of the in situ AFM). Before image analysis, second-order 'flattening' was applied to each image. Roughness was determined using Nanoscope analysis software.

**EQCM.** EQCM measurements were performed using a CHI 420C instrument (Shanghai Chenhua) in a glovebox, and a special electrolytic cell (Supplementary Fig. 3 and Supplementary Section 2). The AT-cut quartz crystals coated by a gold electrode (frequency of 8 MHz), a platinum electrode and a Ag/AgCl electrode were used as the working electrode, counterelectrode and reference electrode, respectively. The surface area of the gold electrode on quartz crystals available for loading the samples was 0.196 $cm^2$. The EQCM experiments were performed at a scan rate of 1 mV $s^{-1}$ in the voltage range 0–3.0 V (OCV is ~3.0 V for a graphite electrode in EQCM), using a standard three-electrode configuration. In this paper we convert all the potentials versus Ag/AgCl to potentials versus $Li/Li^+$ for more convenient comparison. Preparation of the graphite deposited on the gold electrode of the quartz crystals (as a working electrode) is described in the Supplementary Information.

**Environment.** In situ AFM and EQCM were operated in a glovebox, and the oxygen partial pressure and moisture level remained below 0.1 ppm during the entire experimental process.

**DEMS.** DEMS was used to analyse and identify gas evolution during SEI formation on the graphite electrodes. The homemade cell set-up is shown in Supplementary Fig. 7. Using this DEMS cell, we studied gas evolution ($H_2$, $C_2H_4$, $CO_2$ and $O_2$) during the SEI formation process on graphite anode materials in 1 M $LiPF_6$ EC/DMC electrolytes. To avoid interference from a Li-metal anode, which is known to be able to spontaneously reduce the electrolyte and produce gaseous products on cycling, a $LiFePO_4$ electrode was prepared as both reference and counterelectrode, as this remains thermodynamically stable within the electrochemical stability window of the non-aqueous electrolyte. The graphite electrodes and $LiFePO_4$ electrodes (as a reference electrode) were prepared as described in the Supplementary Information.

**Morphology measurement.** The morphologies and thicknesses of the samples were analysed by TEM (FEI Tecnai G2 F30). The cross-sectional sample of the interface was prepared by focused ion beam (FEI, Scios) processing followed by ion beam modulating. Details are provided in the Supplementary Information.

## Data availability

The data that support the plots within this paper and other findings of this study are available from the corresponding author upon reasonable request.